ATLAS Note

Draft version 0.1

Performance Studies of Forward Electron for the HL-LHC

Yassine El Ghazali[a], Mohamed Gouighri[a], Stéphane Jézéquel[b]

[a]*Ibn-Tofail University, Faculty of sciences Kenitra*
[b]*LAPP, Annecy*

This note describes an algorithm used for the reconstruction of electrons in the forward region of the ATLAS detector during the High-Luminosity (HL) phase of the Large Hadron Collider (LHC). This algorithm will benefit from the tracking information provided for the first time by the new Inner Tracker (ITk) alongside the calorimeter information. The ITk will be installed during the Long Shutdown 3 (LS3) which is currently planned to last from 2025 until mid 2027.

Contents

1 Introduction

The detection of particles interacting electromagnetically, such as electrons and photons takes place in the electromagnetic calorimeter (ECAL). A significant amount of their energy is deposited within few cells in the ECAL forming clusters. The forward region of the calorimeter starts from $\eta = 2.5$ where the granularity differs from the barrel part and there is no tracker nowdays. The region up to $\eta=4$ is splitted in two regions with different granularities :

- the inner wheel of the End-Cap electromagnetic calorimeter (EMEC) : $2.5 < \eta < 3.2$

- the Forward Calorimeter (FCAL) : $3.35 < \eta < 4.5$

A transition region for $3.2 < \eta < 3.35$ is also created but will be hardly used for the electron identification. At High-Luminosity LHC (HL-LHC), the ATLAS Collaboration will replace the Inner Tracker called ITk a new Inner tracker which will extend the tracking coverage to a pseudo-rapidity of 4. It will allow to extend the cluster-tracker matching for electron ID from $\eta=2.5$ to 4.0 to separate electrons from jets in the forward region of the ATLAS detector.

The geometry description contains the HGTD material but no reconstructed information is available for the analysis presented in this note.

This note presents an algorithm used for the identification of forward electrons. A preselection is implemented applying cut-based matching criteria based on the angular distances $\Delta\eta$ and $\Delta\phi$ between the cluster and an associated track. As a second step, a multivariate technique based only on cluster shape variables is used to further improve the identification. Results will be presented without Pileup events (PU) or with. In the last case, a $\mu=200$ is applied including intime and out-of-time bunch-crossing PU.

2 The Inner Tracker

The New Inner Tracker (ITk) will be installed during the phase-II Upgrade of the LHC. It will combine precision central tracking in the presence of an average of 200 pile-up events with the ability to extend the tracking coverage to a pseudo-rapidity of 4 while maintain excellent tracking efficiency and performance. The ITK comprises two subsystems: a strip Detector surrounding a Pixel Detector. The Strip Detector has four barrel layers and six end-cap petal-design disks, both having double modules each with a small stereo angle to add $z(R)$ resolution in the barrel(end-caps), respectively. The strip Detector, covering $|\eta| \leq 2.7$, is complemented by a 5 layers Pixel Detector extending the coverage to $|\eta| \leq 4$. The Pixel and Strip Detector volumes are separated by a Pixel Support Tube (PST). in addition, and because of the harsh radiation environment expected for the HL-LHC, the inner two layers of the Pixel Detector are replaceable.The inner two pixel layers are separated from the outer three layers by an Inner Support Tube (IST), that facilitates a replacement of the inner layers. The combined Strip plus Pixel Detectors provide a total of 13 hits for $|\eta| \leq 2.7$ with the exception of the barrel/end-cap transition of the Strip Detector, where the hit count is 11 hits [1]. Figure 1 shows a layout of the ITk, it's is based on one of the candidate layouts described in the Strip TDR called "Inclined Layout" [2].
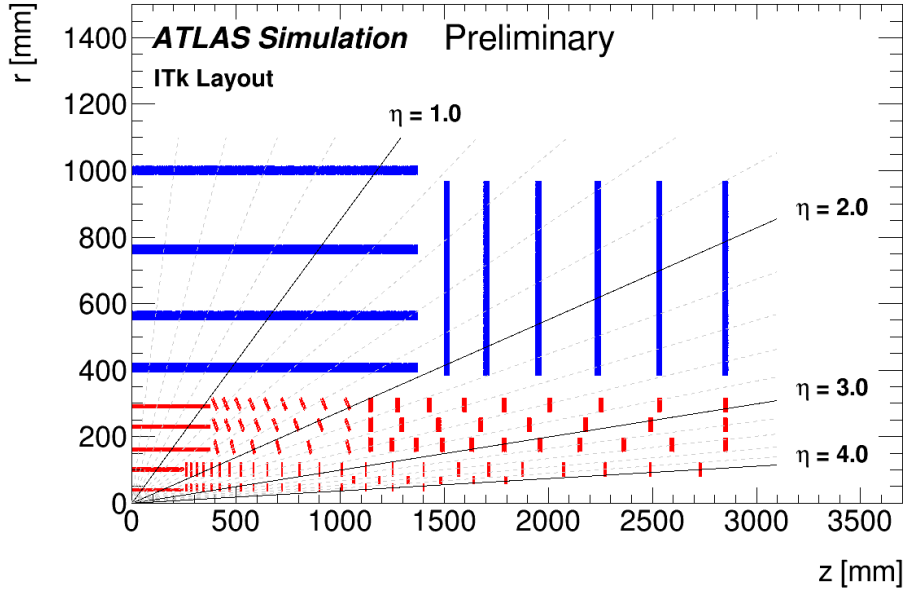
Figure 1: Schematic layout of the ITk Layout for the Phase-II upgrade of ATLAS. The horizontal axis is along the beam line with zero being the interaction point. The vertical axis is the radius measured from the interaction region.

3 Monte Carlo Simulated Samples

The simulated signal samples used for this study were single electron samples, with transverse momenta of 10 and 100 GeV. They were generated using release 21.9 both without any addition of pile-up events, and with a 200 simulated pile-up events. The ITk geometry is ATLAS-P2-ITK-22-02-00. The HGTD material is included in this geometry. The background samples consists of Dijet samples. The list of samples used for this study are listed in Table 1.

Sample	Name
Single e p_T = 10 GeV without PU	mc15_14TeV.900035.PG_singleel_Pt10_etaFlatnp0_43.recon.AOD.e8185_s3595_s3600_r12064
Single e p_T = 100 GeV without PU	mc15_14TeV.900035.PG_singleel_Pt100_etaFlatnp0_43.recon.AOD.e8185_s3595_s3600_r12064
Single e p_T = 10 GeV with PU	mc15_14TeV.900035.PG_singleel_Pt10_etaFlatnp0_43.recon.AOD.e8185_s3595_s3600_r12063
Single e p_T = 100 GeV with PU	mc15_14TeV.900035.PG_singleel_Pt100_etaFlatnp0_43.recon.AOD.e8185_s3595_s3600_r12063
Dijet 20<p_T ≤ 60 GeV	mc15_14TeV.800291.Py8EG_A14NNPDF23LO_jetjet_JZ1WithSW.recon.AOD.e8185_s3595_s3600_r12065
Dijet 60<p_T ≤ 160 GeV	mc15_14TeV.800292.Py8EG_A14NNPDF23LO_jetjet_JZ2WithSW.recon.AOD.e8185_s3595_s3600_r12065

Table 1: Signal and background simulated samples.

4 Track-Cluster Association

In this note, the forward electron identification at HL-LHC relies on both tracker and calorimeter informations. The selection procedure starts by requesting track-cluster angular matching. Only EM clusters in the forward region are matching with a track reconstructed by the ITk algorithms within a minimal distance ΔR are considered.

The clusters in each event are required to have a $p_T > 10$ GeV and is reduced to 5 GeV for the tracks. The tracks that pass this p_T threshold are then extrapolated from perigee to different calorimeter layers in order to correct the offset seen in $\Delta\phi$ distribution. In order to keep only one forward electron candidate per event, the cluster with the highest energy is kept among the ones matching with a track.

In order to speed up the processing, only candidate clusters close to the generated electron within a distance ΔR less than 0.5 are considered for the single electron sample, .

Rather than cutting on ΔR between the cluster and the track, separate cuts on $\Delta\eta$ and $\Delta\phi$ are applied to keep the signal efficiency high as much as possible. Since the granularities of the EM Small Wheel and Forward calorimeter are different, different cuts have to be defined. Therefore, the two regions have been treated differently. So the whole region is divided to 3 separate regions; region covered by the EndCap calorimeters corresponding to 2.5 < η < 3.2, region covered by the Forward calorimeters corresponding to 3.35< η <4.0, and finally the transition region between the EndCap and Forward calorimeters which corresponding to 3.2 < η < 3.35. The table 2 shows the cuts used.

$|\eta|$	2.5 - 3.2	3.2 - 3.35	3.35 - 4.0
$\Delta\eta$	-0.10 - 0.08	-0.04 - 0.08	-0.06 - 0.11
$\Delta\phi$	-0.03 - 0.05	0.03 - 0.05	-0.08 - 0.08

Table 2: $\Delta\eta$ and $\Delta\phi$ selections criteria.

Figures 2 and 3 display the $\Delta\eta$ and $\Delta\phi$ between the track extrapolation on the calorimeter and the cluster for 10 and 100 GeV single electrons without and with pileup as well as dijet background. Two peaks appear in $\Delta\phi$ distribution for single electrons when pileup impact is null or negligible. The shapes are identical between electrons and positrons. The two peaks are disentangled when splitting η positive and negative. A similar issue had been observed in Run 2 data, you can check this reference for more details.
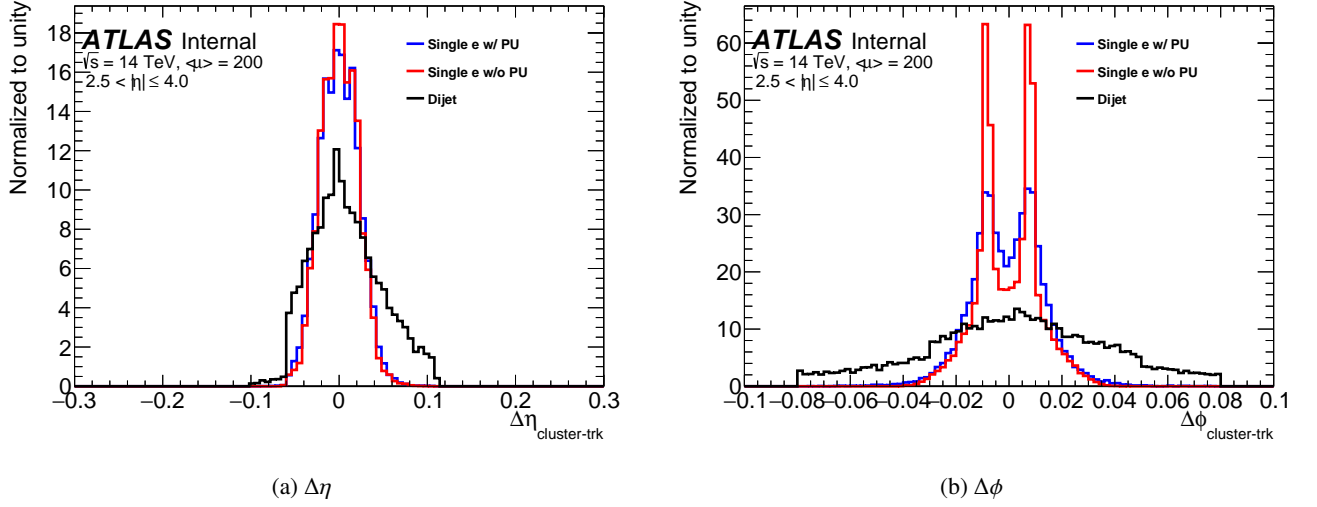
(a) $\Delta\eta$

(b) $\Delta\phi$

Figure 2: Comparison of the angular distances $\Delta\eta$ (left) and $\Delta\phi$ (right) between the cluster and its closest track, simulated single electron with $p_T = 100$ GeV without pile-up is shown in red color, the blue color corresponds to single electron with pile-up and the black for Dijets with ($20 \leq p_T \leq 60$ GeV).
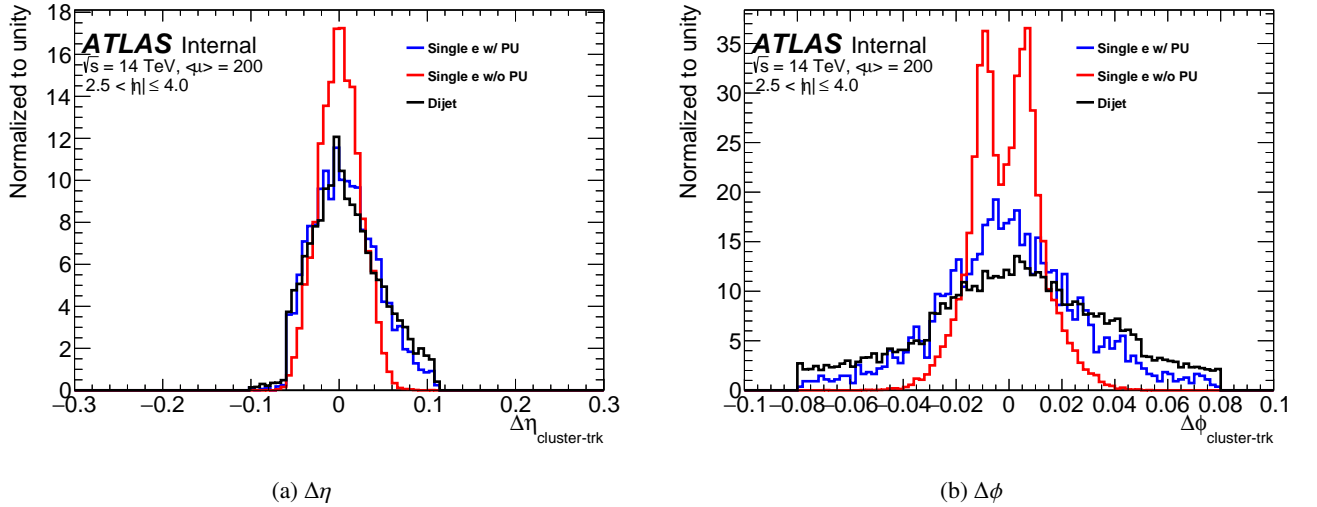

(a) $\Delta\eta$

(b) $\Delta\phi$

Figure 3: Comparison of the angular distances $\Delta\eta$ (left) and $\Delta\phi$ (right) between the cluster and its closest track, simulated single electron with $p_T = 10$ GeV without pile-up is shown in red color, the blue color corresponds to single electron with pile-up and the black for Dijets with ($20 \leq p_T \leq 60$ GeV).

As it was mentioned before in order to correct the offset in 2(b) and 3(b), the track has been extrapolated to the calorimeter layers using a tool called `CaloExtension`. To illustrate the impact of the track extrapolation, both $\Delta\eta$ and $\Delta\phi$ distributions before and after track extrapolation to the calorimeter are displayed in figures 4 and 5.
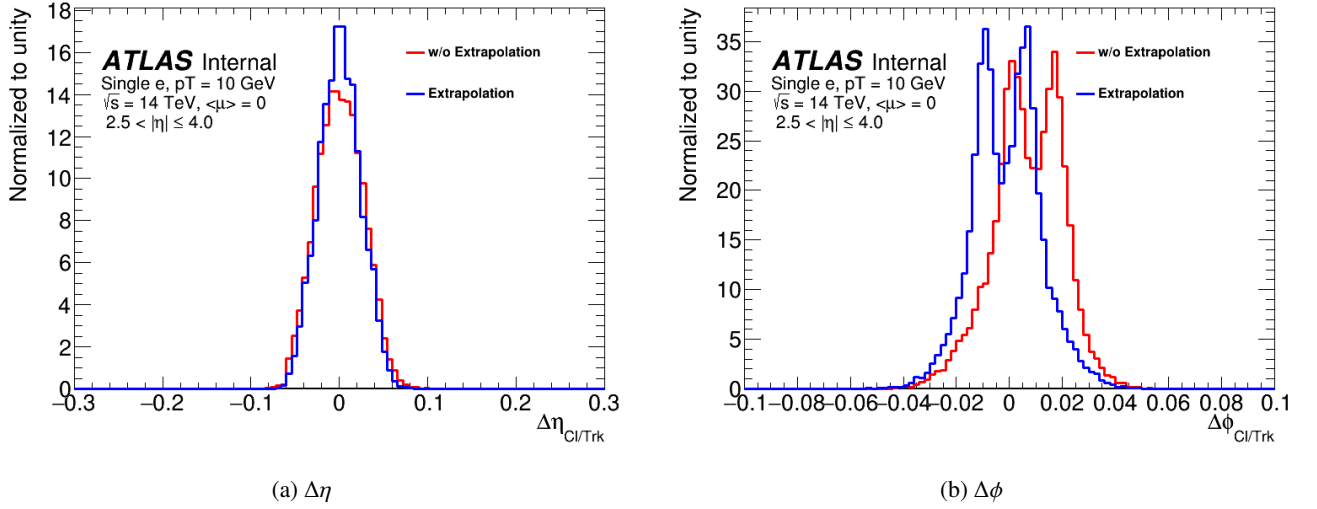
(a) $\Delta\eta$

(b) $\Delta\phi$

Figure 4: Comparison of the angular distances $\Delta\eta$ (left) and $\Delta\phi$ (right) between the cluster and its closest track before and after extrapolating the track, for simulated single electron with $p_T = 10$ GeV without pile-up.
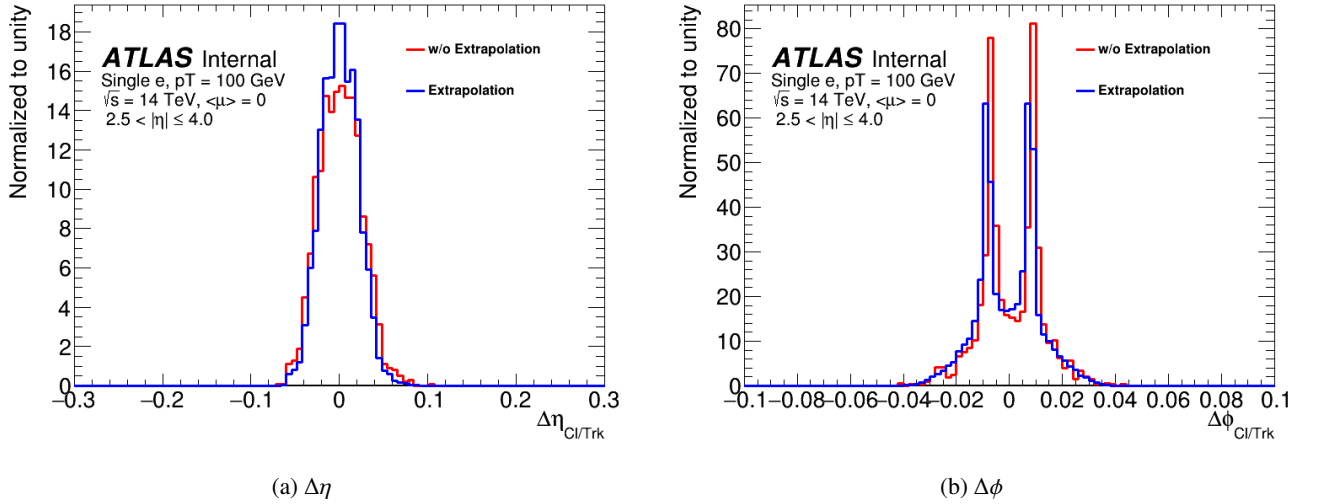

(a) $\Delta\eta$

(b) $\Delta\phi$

Figure 5: Comparison of the angular distances $\Delta\eta$ (left) and $\Delta\phi$ (right) between the cluster and its closest track before and after extrapolating the track, for simulated single electron with $p_T = 100$ GeV without pile-up.

5 Cluster shape based identification

As the current Inner Detector doesn't provide the tracking information for forward electrons, so the reconstruction algorithm deals only with clusters. Because of this the reconstruction algorithm can't make a difference between electrons and photons, and electrons and positrons. For this region an-other cluster-construction algorithm is used which is called "topological clustering", this algorithm use the

105 cluster shape variables for the identification of these electron, which means that the cuts are applied to the
106 cluster itself, and take into account such parameters as longitudinal second momentum, transverse second
107 momentum, normalized lateral momentum and so on.

108 The 6 variables which are used to define the shape of a cluster are highlighted in the table 3

Name	Description	Variable
Shower depth	The distance of the shower barycenter from the calorimeter front face measured along the shower axis	λ_{center}
Maximum cell energy	Fraction of the cluster energy in the most energetic cell	f_{max}
Longitudinal second momentum	Second momentum of the distance of each cell to the shower center in the longitudinal direction (λ_i)	$<\lambda^2>$
Transverse second momentum	Second momentum of the distance of each cell to the shower center in the transverse direction (r_i)	$<r^2>$
Normalized lateral momentum	Calculated as $\frac{w_2}{w_2+w_{max}}$ where w_2 and w_{max} are second momenta of r_i for different weights per cell	w_{norm}
Normalized longitudinal momentum	Calculated as $\frac{\lambda_2}{\lambda_2+\lambda_{max}}$ where λ_2 and λ_{max} are second momenta of λ_i for different weights per cell	λ_{norm}

Table 3: The shower shape variables used in the forward electron identification.

6 Multivariate technique

110 The multivariate approach uses both the track-cluster matching variables and the 6 cluster shape variables.
111 Two different methods have been implemented: the Boosted Decision Tree (BDT) and Artificial Neural
112 Network (ANN). The training, specific to the End-Cap Inner Wheel and the Forward calorimeters was done
113 in a previous study [3], and has included only the End-Cap and the Forward calorimeters. The transition
114 region ($3.2 < |\eta| < 3.35$) was excluded due to low performances induced by the distance between the two
115 regions.

116 Three working points have been defined: loose, medium and tight corresponding to 90%, 80% and 70% of
signal efficiency respectively. Their definitions are summarized in Table 4.

$|\eta|$	$|\eta| \leq 3.2$	$|\eta| \geq 3.35$	$|\eta| \leq 3.2$	$|\eta| \geq 3.35$
Loose	-0.045 < BDT < 0.095	-0.365 < BDT < 0.125	0.375 < NN < 0.795	0.365 < NN < 0.855
Medium	0.095 < BDT < 0.165	0.125 < BDT < 0.195	0.795 < NN < 0.915	0.855 < NN < 0.932
Tight	BDT > 0.165	BDT > 0.195	NN > 0.915	NN > 0.932

Table 4: Definitions of Loose, Mediun and Tight operating points.

117

7 Results

7.1 Electrons

7.1.1 Reconstruction Efficiencies

The total reconstruction efficiencies for simulated single electrons samples with $p_T = 10$ GeV are shown in Figure 6 and for 100 GeV sample in Figure 7. The signal efficiency for electrons with $p_T = 100$ GeV is above 70% in all η region except the transition region ($3.2 < |\eta| < 3.35$) between the End-Caps and the Forward calorimeters, where it is expected to be lower due to the geometry

Adding 200 simulated interaction pile-up per bunch crossing on top of single electrons degrades the selection efficiency especially for low p_T electrons. While the fake probability is shown in figure 8. Tables 5 and 6 summarize the signal efficiency of signal electron samples as well as the fake rate with and without pile-up obtained using Neural Network (NN) and Boosted Decision Tree (BDT) respectively.

Working-point	Loose	Medium	Tight
No simulated pile-up interaction			
Single e $p_T = 10$ GeV	61.54 ± 0.26	56.52 ± 0.26	49.32 ± 0.26
Single e $p_T = 100$ GeV	88.24 ± 0.17	83.82 ± 0.19	76.48 ± 0.22
200 simulated pile-up interactions			
Single e $p_T = 10$ GeV	8.40 ± 0.15	5.32 ± 0.12	4.11 ± 0.1
Single e $p_T = 100$ GeV	82.56 ± 0.20	76.91 ± 0.23	69.01 ± 0.25
Dijet	1.74 ± 0.06	0.72 ± 0.04	0.48 ± 0.03

Table 5: Neural Network selection efficiency in percent. Only statistical errors included.

Working-point	Loose	Medium	Tight
No simulated pile-up interaction			
Single e $p_T = 10$ GeV	60.76±0.26	53.72±0.26	45.19±0.26
Single e $p_T = 100$ GeV	88.38±0.17	83.17 ± 0.20	75.16 ± 0.23
200 simulated pile-up interactions			
Single e $p_T = 10$ GeV	15.15±0.19	5.55±0.12	4.03±0.10
Single e $p_T = 100$ GeV	82.94 ±0.20	75.07 ± 0.23	66.06±0.25
Dijet	7.32± 0.12	0.63±0.03	0.36± 0.02

Table 6: Boosted Decision Tree selection efficiency in percent. Only statistical errors included.
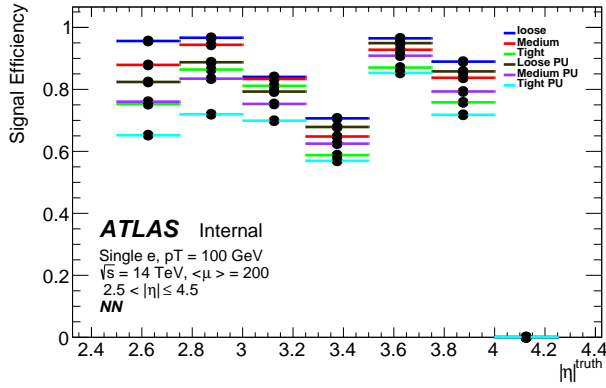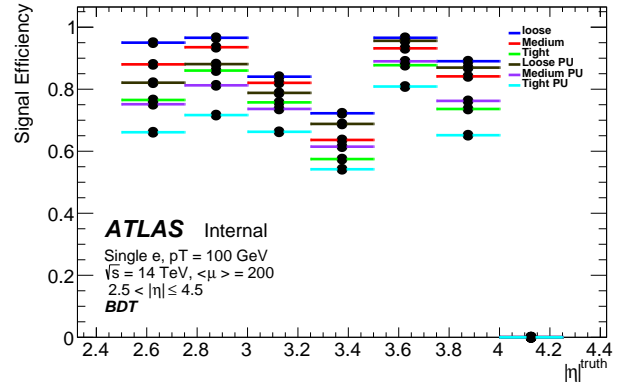
Not reviewed, for internal circulation only
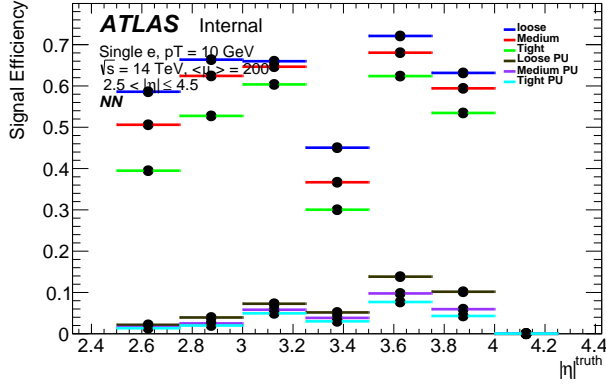
(a) NN
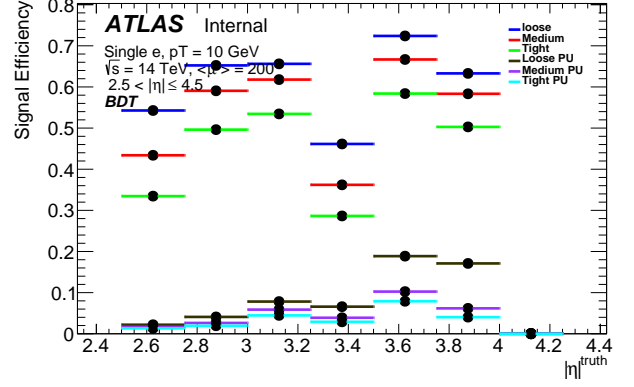
(b) BDT

Figure 6: The total reconstruction efficiency for simulated single electrons with p_T = 10 GeV with and without pile-up is shown as a function of true η NN (a) and BDT (b).
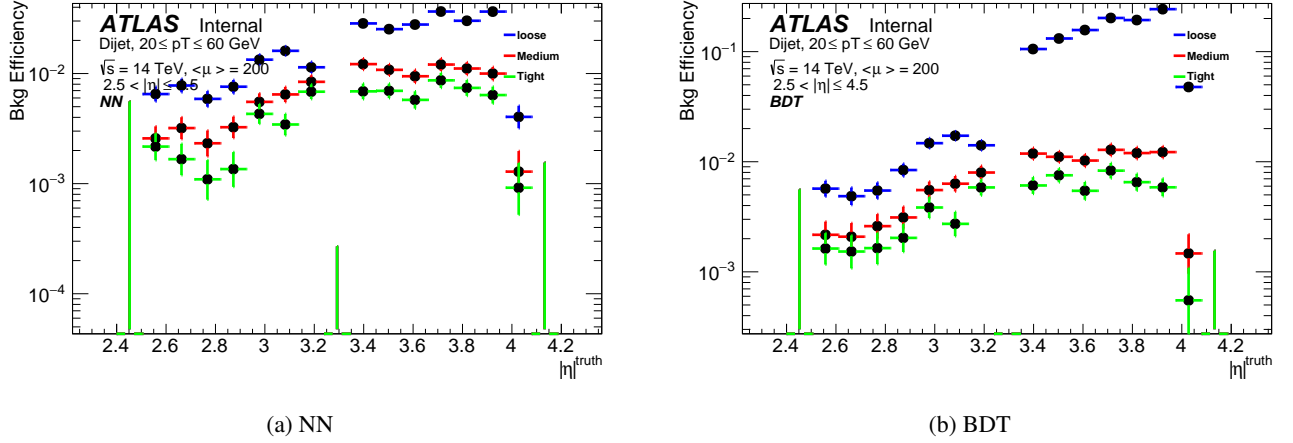

(a) NN

(b) BDT

Figure 7: The total reconstruction efficiency for simulated signle electrons with p_T = 100 GeV with and without pile-up is shown as a function of true η NN (a) and BDT (b).

(a) NN

(b) BDT

Figure 8: The total jet fake probability as a function of $|\eta|^{truth}$ NN (a) and BDT (b).

7.1.2 Charge Mis-Identification Probability

A measurement of the probability of charge misidentification is performed using a single electron sample. The probability for an electron to be reconstructed with the wrong charge is obtained from the number of events where both the reconstructed and generated electrons have opposite electric charge. Figures 9 and 10 show the charge mis-identification rates as a function of $|\eta|$ in a single electron sample with $p_T = 10$ GeV and $p_T = 100$ GeV respectively.

Working-point	Loose	Medium	Tight
Single e $p_T = 10$ GeV	0.07±0.01	0.02±0.009	0.014±0.008
Single e $p_T = 100$ GeV	2.08±0.07	1.95±0.07	1.74±0.07

Table 7: Charge mis-identification probability of single e with pile-up using NN method, Only statistical errors included.

Working-point	Loose	Medium	Tight
Single e $p_T = 10$ GeV	0.22±0.02	0.02±0.009	0.011±0.007
Single e $p_T = 100$ GeV	2.08±0.07	1.89±0.07	1.66±0.07

Table 8: Charge mis-identification probability of single e with pile-up using BDT method, Only statistical errors included.

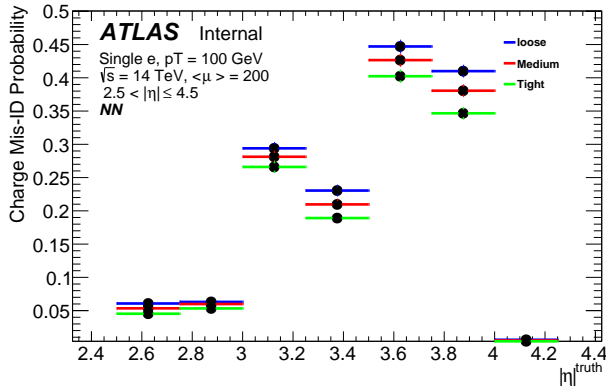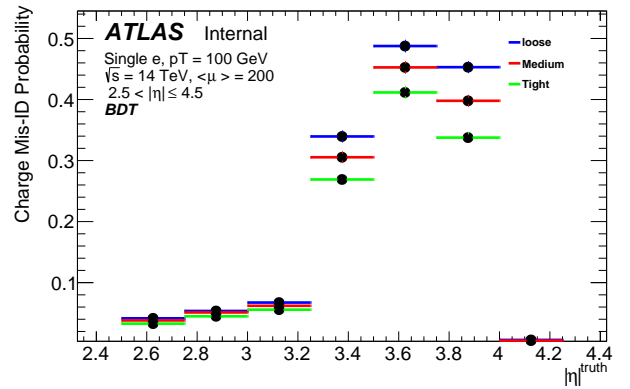Not reviewed, for internal circulation only
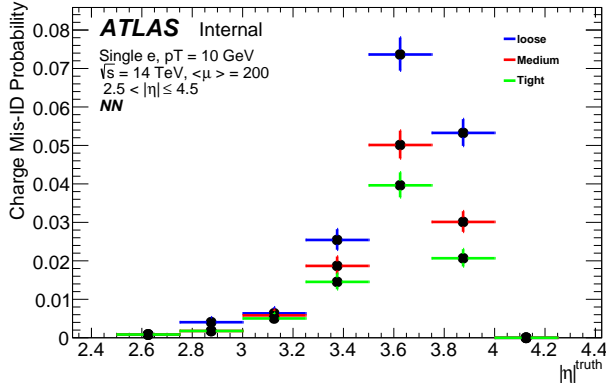
(a) NN
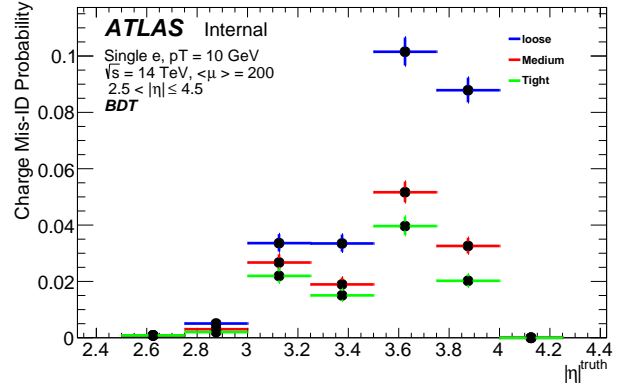
(b) BDT

Figure 9: Charge-misidentification rates as function of $|\eta|$ in a single-electron sample with $p_T = 10$ GeV is shown as a function of the true η left NN and right BDT.

(a) NN

(b) BDT

Figure 10: Charge-misidentification rates as function of $|\eta|$ in a single-electron sample with $p_T = 100$ GeV is shown as a function of the true η left NN and right BDT.

7.2 Pile-up noise

The HL-LHC will operate at an instantaneous luminosity up to $\mathcal{L} = 7.5 \times 10^{34} cm^{-2} s^{-1}$ which corresponds to an average of approximately 200 inelastic proton-proton collisions per beam crossing. Despite the optimization of the ITk in order to cope with these requirements, and to maintain the same tracking performance as the present ATLAS Inner Detector, some of the pile-up events could fulfil the selections and therefore reconstructed as a true electrons.

In this section an estimation of these events is performed by requiring the reconstructed electron to be in the opposite region of the true electron, i.e. $\eta(Reco) \times \eta(truth) \leq 0$, figures 11 and 12 show the probability as function of $|\eta|$ of pile-up events to pass the selections and to be reconstructed as a true electron for 10 and 100 GeV samples respectively.
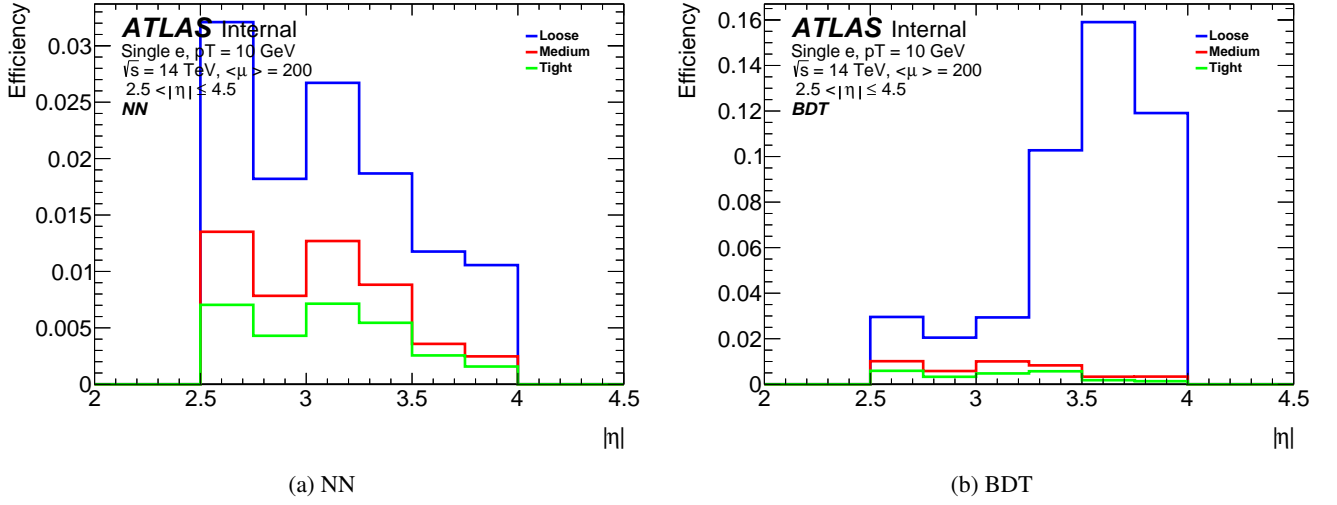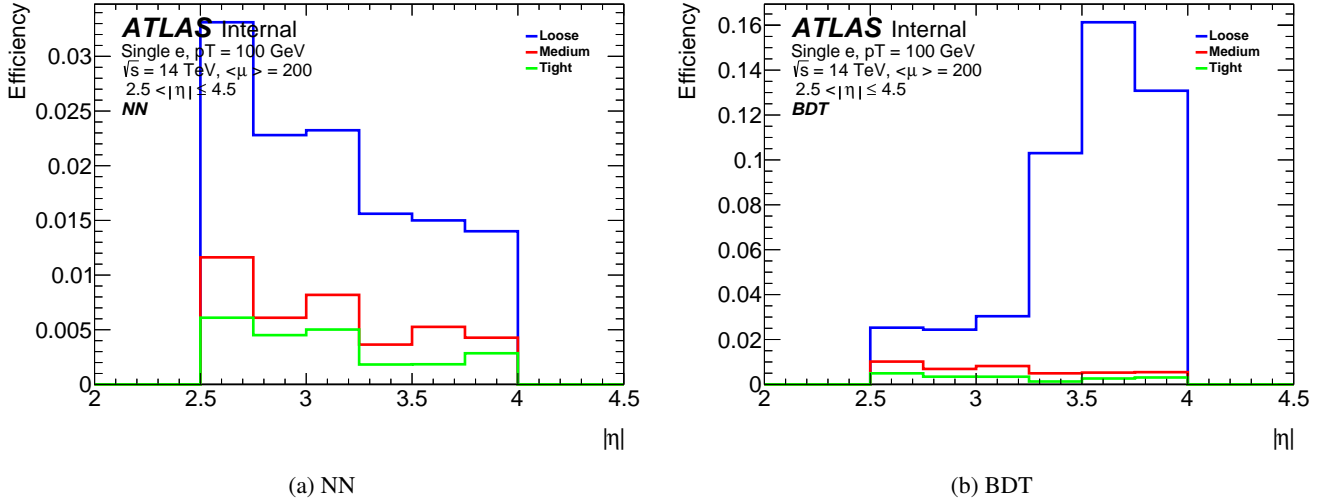
(a) NN

(b) BDT

Figure 11: The probability to reconstruct a pile-up event as an electron in a single-electron sample with $p_T = 10$ GeV is shown as a function of $|\eta|$ left NN and right BDT for $< \mu >= 200$.

(a) NN

(b) BDT

Figure 12: The probability to reconstruct a pile-up event as an electron in a single-electron sample with $p_T = 100$ GeV is shown as a function of $|\eta|$ left NN and right BDT for $< \mu >= 200$.

8 Conclusion

As part of the Phase-II upgrade, the current ATLAS Inner Detector will be replaced by the ITk to meet the challenges of the HL-LHC environment, as well as to provide tracking information for forward electrons. The study showed that the cluster-track matching has the ability to identify electrons and reject the jets and pile-up that could mimic the reconstruction. Three working points (Loose, Medium and Tight) have been evaluated on Monte-Carlo samples with $< \mu >= 0$ and $< \mu >= 200$.

References

[1] A. Collaboration, *Technical Design Report for the ATLAS Inner Tracker Pixel Detector*, CERN-LHCC-2017-021, 2017, URL: https://cds.cern.ch/record/2285585 (cit. on p. 3).

[2] A. Collaboration, *Technical Design Report for the ATLAS Inner Tracker Strip Detector*, CERN-LHCC-2017-005, 2017, URL: https://cds.cern.ch/record/2257755 (cit. on p. 3).

[3] P. Bellos, C. Anastopoulos, D. Fassouliotis, C. Kourkoumelis and K. Nikolopoulos, *Forward Electron Identification for the HL-LHC ATLAS Detector*, en, () 25, URL: https://cds.cern.ch/record/2308701 (cit. on p. 8).

Not reviewed, for internal circulation only

Appendices

A Comparison between ITk-22 and ITk-23 geometries

This chapter shows a comparison between two different ITk geometries; the geometry ATLAS-P2-ITK-22-02-00 with which the results shown in this note have been produced and the geometry ATLAS-P2-ITK-23-00-01 which contains more material compared to the oldest tag especially in Outer Barrel.

A.1 Angular distributions

(a) $\Delta\eta$

(b) $\Delta\phi$
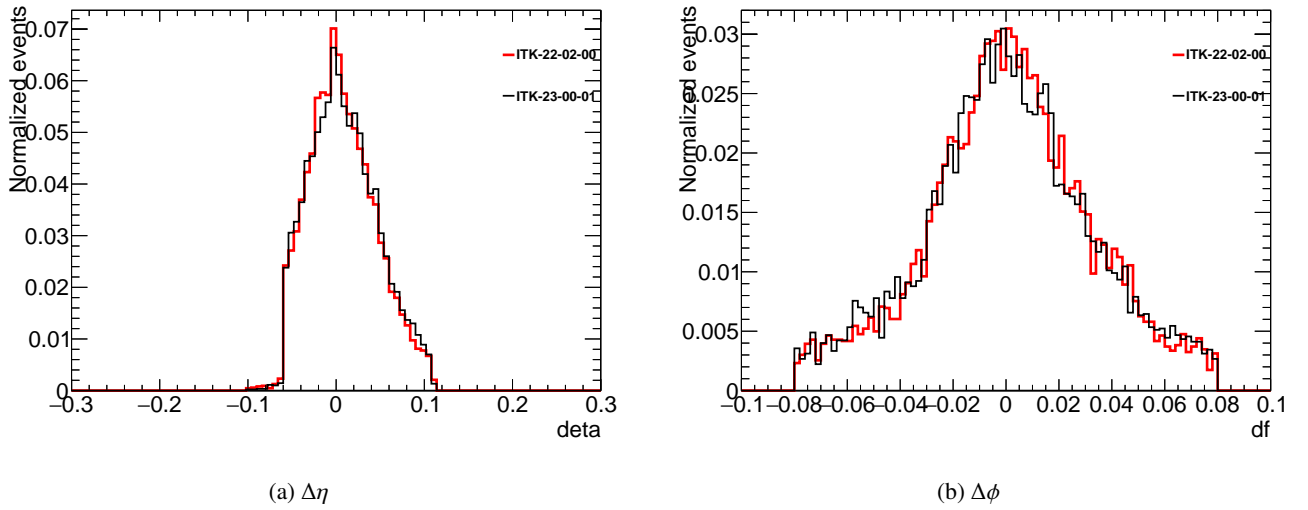
Figure 13: $\Delta\eta$ (left) and $\Delta\phi$ (right) comparison for 10 GeV sample without pile-up between ATLAS-P2-ITK-22-02-00 (red) and ATLAS-P2-ITK-23-00-01 (blue) .
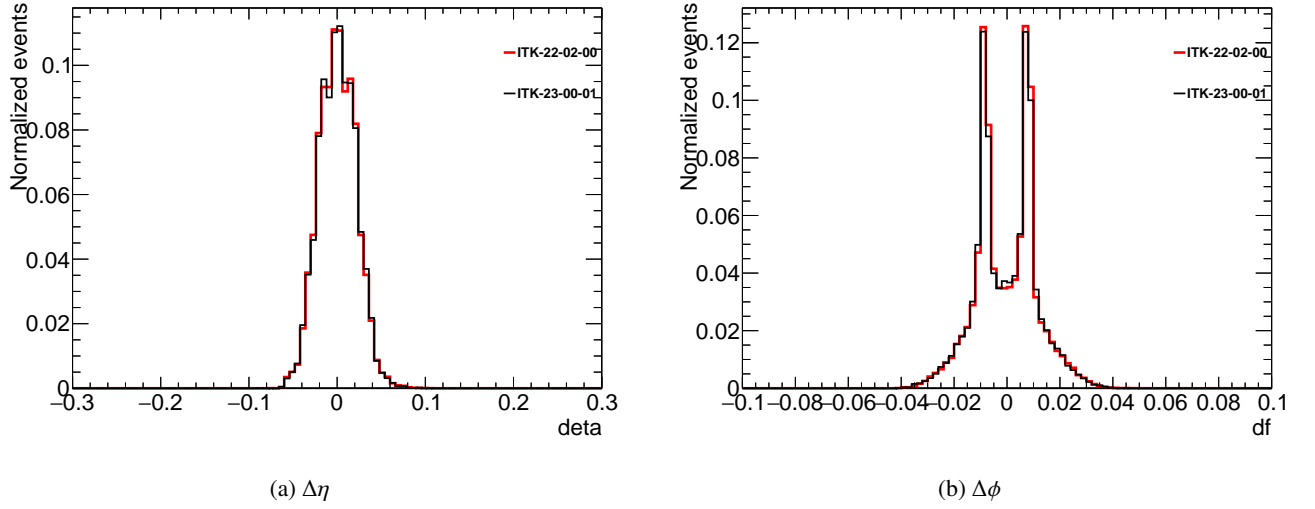
(a) $\Delta\eta$

(b) $\Delta\phi$
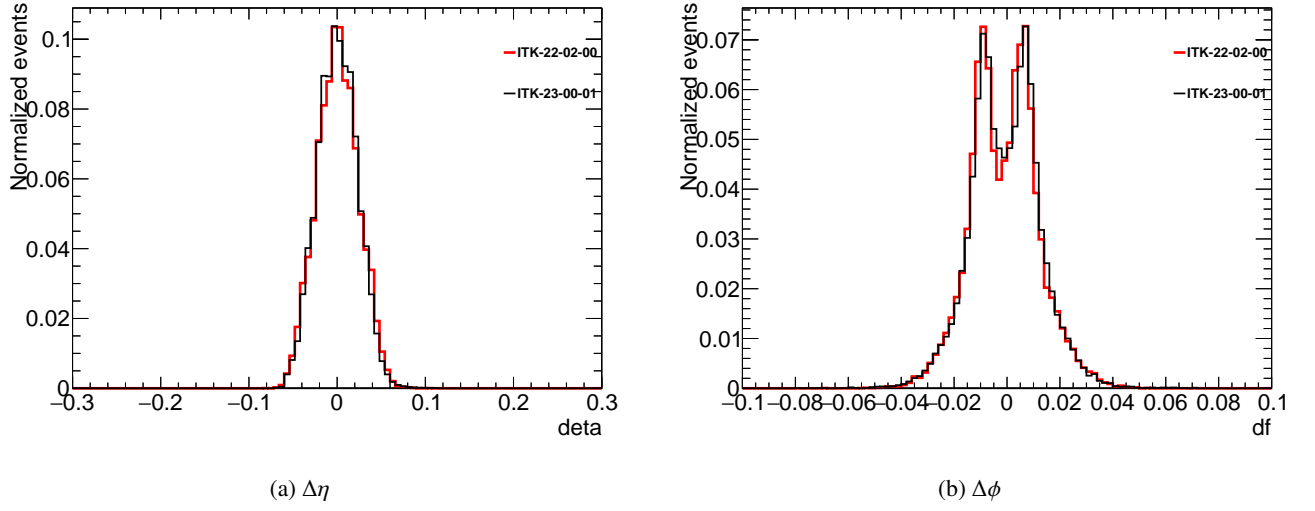
Figure 14: $\Delta\eta$ (left) and $\Delta\phi$ (right) comparison for 10 GeV sample with pile-up between ATLAS-P2-ITK-22-02-00 (red) and ATLAS-P2-ITK-23-00-01 (blue) .

(a) $\Delta\eta$

(b) $\Delta\phi$
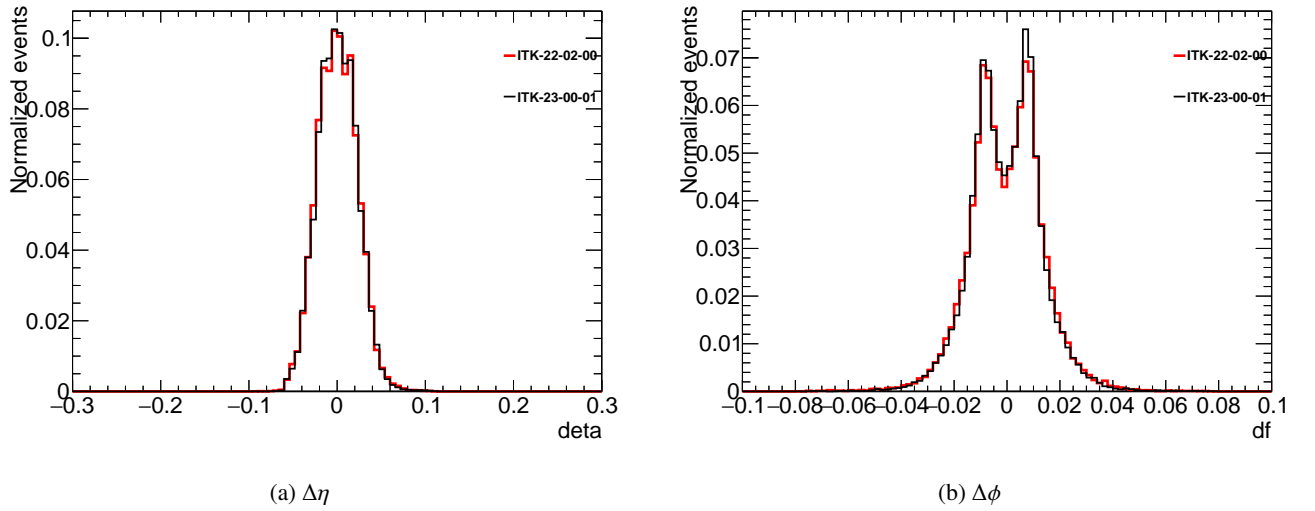
Figure 15: $\Delta\eta$ (left) and $\Delta\phi$ (right) comparison for 100 GeV sample without pile-up between ATLAS-P2-ITK-22-02-00 (red) and ATLAS-P2-ITK-23-00-01 (blue) .

(a) $\Delta\eta$

(b) $\Delta\phi$

Figure 16: $\Delta\eta$ (left) and $\Delta\phi$ (right) comparison for 100 GeV sample with pile-up between ATLAS-P2-ITK-22-02-00 (red) and ATLAS-P2-ITK-23-00-01 (blue) .

A.2 Reconstruction efficiency comparison

(a) $< \mu >= 0$
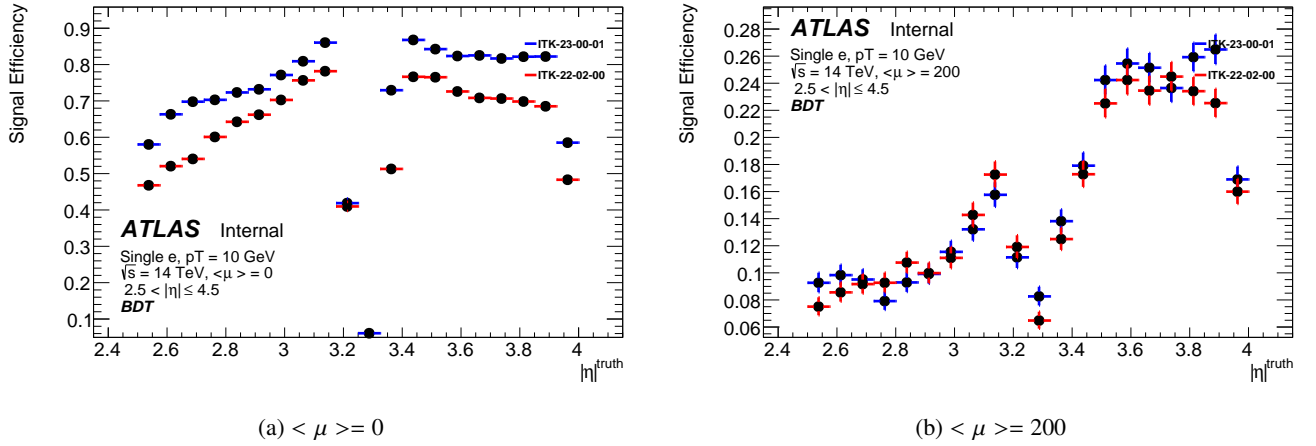
(b) $< \mu >= 200$

Figure 17: Signal efficiency comparison for 10 GeV sample without pile-up (left) and with 200 simulated pile-up (right) between ATLAS-P2-ITK-22-02-00 (red) and ATLAS-P2-ITK-23-00-01 (blue) .
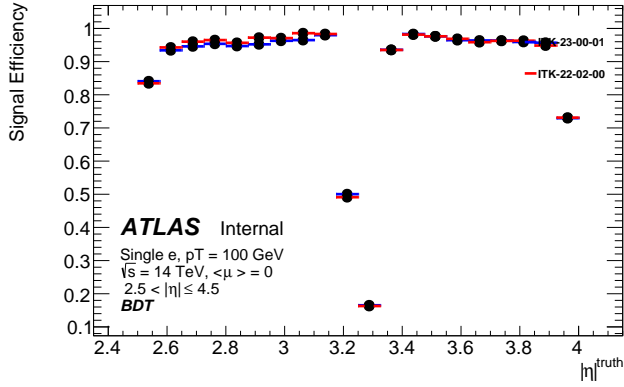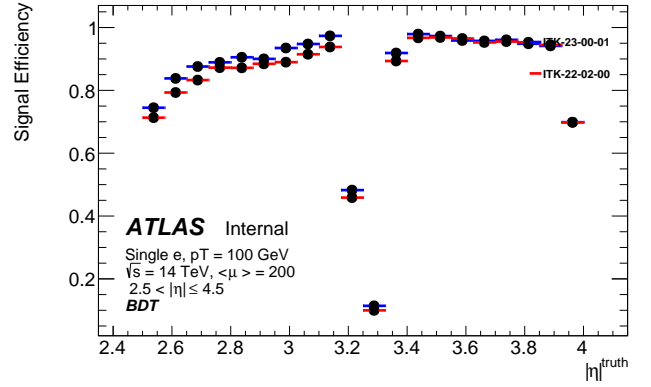
(a) $< \mu >= 0$

(b) $< \mu >= 200$

Figure 18: Signal efficiency comparison for 100 GeV sample without pile-up (left) and with 200 simulated pile-up (right) between ATLAS-P2-ITK-22-02-00 (red) and ATLAS-P2-ITK-23-00-01 (blue) .
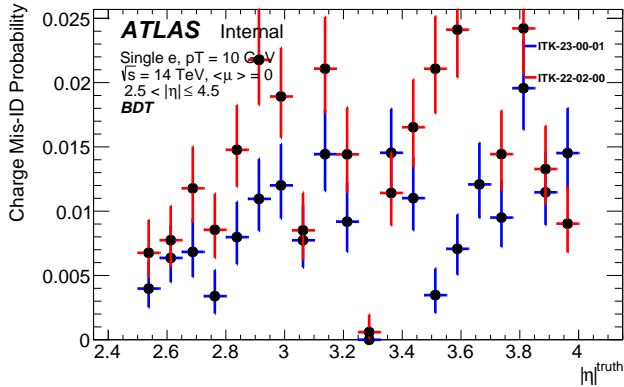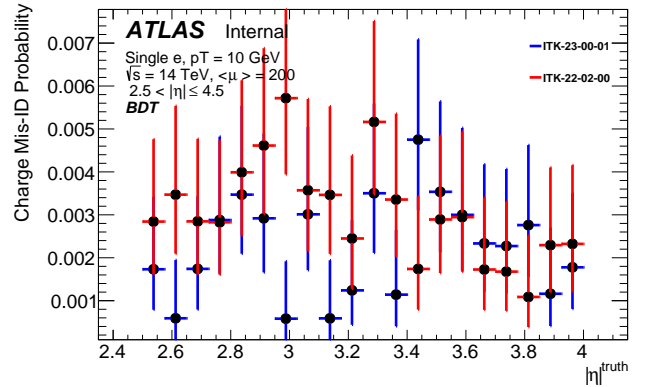
A.3 Charge mis identification probability

(a) $< \mu >= 0$

(b) $< \mu >= 200$

Figure 19: Charge mis-ID probability comparison for 10 GeV sample without pile-up (left) and with 200 simulated pile-up (right) between ATLAS-P2-ITK-22-02-00 (red) and ATLAS-P2-ITK-23-00-01 (blue) .
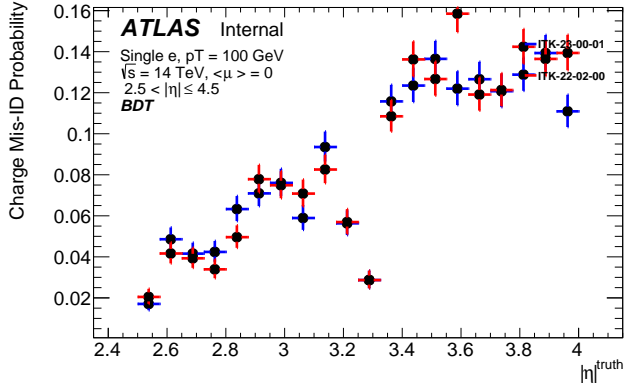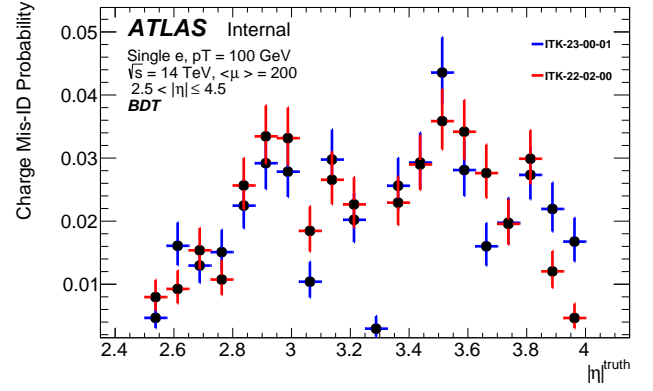
Not reviewed, for internal circulation only

(a) $<\mu>= 0$ (b) $<\mu>= 200$

Figure 20: Charge mis-ID probability comparison for 100 GeV sample without pile-up (left) and with 200 simulated pile-up (right) between ATLAS-P2-ITK-22-02-00 (red) and ATLAS-P2-ITK-23-00-01 (blue) .